Electrochemical Potassiation/Depotassiation Properties of Rare-Earth Antimonide/Antimony Composite Electrodes

Yasuhiro Domi,*[,†,§] *Hiroyuki Usui*,[†,§] *Naoya Wada,*[‡,§] *Takayuki Yamamoto*,[⊥] *Toshiyuki Nohira*,[⊥] *Kei Nishikawa,*[∥] *and Hiroki Sakaguchi**[,†,§]

[†]Department of Chemistry and Biotechnology, Graduate School of Engineering, Tottori University, Minami 4–101, Koyama–cho, Tottori 680–8552, Japan

[‡]Course of Chemistry and Biotechnology, Department of Engineering, Graduate School of Sustainability Science, Tottori University, Minami 4–101, Koyama–cho, Tottori 680–8552, Japan

[§]Center for Research on Green Sustainable Chemistry, Tottori University, Minami 4–101, Koyama–cho, Tottori 680–8552, Japan

[⊥]Institute of Advanced Energy, Kyoto University, Uji 611–0011, Japan

[∥]International Center of Young Scientists, National Institute for Materials Science, 1–1 Namiki, Tsukuba 305–0044, Japan

domi@tottori-u.ac.jp, usui@tottori-u.ac.jp, tottori.naoya@gmail.com, yamamoto.takayuki.2w@kyoto-u.ac.jp, t-nohira@iae.kyoto-u.ac.jp, NISHIKAWA.Kei@nims.go.jp, sakaguch@tottori-u.ac.jp

*Corresponding Authors

Yasuhiro Domi Tel/Fax: +81-857-31-5249, E-mail: domi@tottori-u.ac.jp

Hiroki Sakaguchi Tel/Fax: +81-857-31-5048, E-mail: sakaguch@tottori-u.ac.jp

ABSTRACT (217/300 words)

Potassium-ion batteries have emerged as promising next-generation energy storage systems due to the abundance and low cost of potassium. However, achieving high capacity and long-term cycling stability remains a challenge, especially for metal/alloy anodes such as antimony (Sb), which suffers from significant volume changes during charge–discharge cycling. To address this, we developed composite anodes combining Sb with rare-earth antimonides ($RESb_x$), known for their charge-discharge cycle stability. The electrochemical performances of $RESb_x$/Sb composite electrodes were systematically evaluated in an ionic liquid electrolyte. Charge-discharge testing revealed that the addition of $RESb_x$, even at 10 wt.%, significantly suppressed the rapid capacity fading observed in a pure Sb electrode, leading to excellent cycling stability. Additionally, Sb contributed most of the capacity in the composites, whereas the $RESb_x$ component effectively suppressed electrode degradation. Particularly, a CeSb/Sb electrode maintained over three times the cycle life of the pure Sb electrode. Cross-sectional scanning electron microscopic analysis demonstrated that the $RESb_x$ phase mitigated electrode expansion and cracking. Further investigation showed that high potassium-ion diffusion coefficient, associated with larger lattice parameters of $RESb_x$, and the mechanical softness (lower breaking strength) of CeSb, played key roles in enhancing cycle life. These properties facilitate uniform K^+ distribution and reduce mechanical stress in the electrode. The findings contribute to the advancement of high-performance and resource-efficient energy storage technologies.

KEYWORDS: potassium-ion batteries; antimony; composite; electrode thickness; K^+ diffusion coefficient; reference breaking strength; ionic liquid electrolyte 5-8 words

1. Introduction

Since their commercialization in 1991, lithium-ion batteries (LIBs) have been widely utilized in various fields, including smartphones and electric vehicles (EVs), due to their high energy density and long cycle life.[1–3] Thus, LIBs have thus become indispensable energy storage devices in modern society. However, lithium, the key component of LIBs, is associated with supply risks and price volatility because of its uneven geographical distribution and high extraction costs. Therefore, developing next-generation rechargeable batteries that use inexpensive, abundant resources instead of lithium is critical.

Sodium-ion batteries (NIBs) have attracted considerable attention as one such alternative, and their commercialization for EV applications is currently underway.[4–7] Sodium has the significant advantage of being abundant on Earth, with fewer resource constraints. To achieve a decarbonized society, it is essential to expand the use of renewable energy with high-performance storage batteries. It is also extremely important to establish a diverse lineup of storage batteries for various applications. In consideration of this backdrop, potassium-ion batteries (KIBs), which employ potassium ions as charge carriers, are highly attractive from a resource perspective, similar to NIBs.[7–10] Furthermore, the low redox potential of K^+/K in organic electrolytes contributes to the potential for high energy density, while the relatively small solvated radius of K^+ is expected to enable excellent rate capabilities.

Although these alkali metal secondary batteries share a common "rocking-chair" mechanism, where monovalent cations shuttle between the cathode and anode, the optimal electrode materials for each battery system vary considerably.[11,12] For instance, graphite is widely used as an anode for LIBs, whereas hard carbon is predominantly used in NIBs due to the difficulty

of Na^+ intercalation into graphene layers.[4–7] Furthermore, our previous studies have indicated that even when using the same active materials, the specific properties required for superior performance differ between NIBs and KIBs.[13] Thus, for the practical realization of KIBs, it is essential to thoroughly investigate the characteristics of diverse electrode active materials and establish a broad portfolio to accommodate diverse applications.

Focusing on anode active materials for KIBs, although graphite demonstrates high Coulombic efficiency and excellent cycle stability[10,14–16], achieving higher energy densities requires the development of compound-based or metal-based electrodes with high theoretical capacities.[17–23] However, these electrodes suffer from poor cycling performance due to the severe volume expansion and contraction during charge and discharge processes, respectively. Our research group has addressed performance improvement in LIB and NIB anodes through multifaceted approaches, including composite formation with other materials,[24–28] alloying or compound formation with different elements,[29–32] and impurity doping.[33–37]

Here, we focus on antimony (Sb) as a promising anode material for KIBs.[10,19] Although the gravimetric theoretical capacity of Sb electrodes (K_3Sb: 660 mA h g^{-1}) is lower than that of phosphorous electrodes (K_4P_3: 1154 mA h g^{-1}), Sb offers a significantly higher volumetric theoretical capacity (K_3Sb: 4422 mA h cm^{-3} vs. K_4P_3: 3104 mA h cm^{-3}), making it an attractive candidate from a practical perspective. Nevertheless, the Sb electrodes undergo a significant volume change (407%) during charge and discharge processes, which generates stress. This leads to strain accumulation over repeated cycles, ultimately causing electrode degradation and capacity fading after a relatively short number of cycles. To overcome this issue, we have synthesized Sb-based alloys and evaluated their anode properties.[13] Our findings revealed that $FeSb_2$ electrodes possessed a commendable balance of relatively high reversible capacity and excellent cycling

stability. Additionally, we demonstrated that rare-earth antimonide (RESb$_x$) electrodes could maintain stable reversible capacity over 500 cycles despite exhibiting lower initial capacity compared to the $FeSb_2$ electrode.

The present study aimed to develop high-performance KIB anodes that achieve both high reversible capacity and long-term cycling stability by composite formation with Sb, which offers high capacity but limited cycle stability, and RESb$_x$, known for its superior cycle stability. We systematically investigated the influence of different rare-earth elements on the anode properties and discussed the effects based on reaction behavior analyses. The findings of this work are expected to provide valuable guidelines for the design of high-performance anode active materials, thereby contributing to the practical realization of KIBs and the broader advancement of next-generation energy storage technologies.

2. Experimental

2.1. Synthesis and Characterization of RESb$_x$/Sb Composites.

RESb$_x$/Sb composites were synthesized as active materials using the mechanical alloying (MA) method by 2-step. Rare-earth used in this study was yttrium (Y), lanthanum (La), cerium (Ce), samarium (Sm), and gadolinium (Gd). Sb powder and Sm chips were purchased from FUJIFILM Wako Pure Chemical Corporation, Ltd. Y powder and Ce ingots were obtained from Nilaco Corporation, Ltd. The shot-like La and Gd supplied by Santoku Corp. were cut into smaller pieces using a nipper and then subjected to a sieve treatment. A mixture of Sb and other elements in a 1:1 molar ratio was enclosed in a stainless-steel container along with stainless-steel balls. The

weight ratio of the mixture to the balls was approximately 1:30. The MA was conducted using a planetary ball-milling apparatus (P-6, Fritsch) at a rotational speed of 380 rpm for 10 h at room temperature. The *RE*Sb_x/Sb composites were obtained by mechanical mixing (MM) of the synthesized *RE*Sb_x with Sb powder at the same rotational speed for 10 min. The entire process from weighing the raw materials to MM process was carried out in a glovebox (Miwa MFG, DBO-2.5LNKP-TS) with an argon atmosphere, ensuring an oxygen content of 1 ppm or less and a dew point below −90°C.

The synthesized composite powders were characterized by X-ray diffraction (XRD; Ultima IV, Rigaku), field emission scanning electron microscopy (FE-SEM; JSM-IT800, JEOL Ltd.), and laser diffraction particle size analyzer (SALD-2300, Shimadzu Co. Ltd.). The XRD measurement was conducted using Cu-Kα radiation at a current of 40 mA and a voltage of 40 kV. Cu or Al was used as an internal standard substance. FE-SEM observation was performed with an accelerating voltage between 5 and 10 kV and a working distance of 10 mm. The particle size analysis was conducted through the following procedure: the composite powder and a neutral detergent were mixed in a weight ratio of approximately 100:1. This mixture was then dispersed in deionized water and gently stirred while preventing the formation of bubbles. The neutral detergent was added to suppress the aggregation of composite particles.

The weight ratio of the obtained composite samples was quantitatively analyzed using wavelength-dispersive X-ray fluorescence (WD-XRF; ZSX Primus, Rigaku) and/or inductively coupled plasma atomic emission spectroscopy (ICP-AES; SPECTRO CIROS CCD). In WD-XRF measurements, Rhodium (Rh) was used as the target materials for the X-ray source, and LiF was employed as the spectroscopic crystal. ICP-AES measurements were conducted under the conditions of plasma power at 1400 W and a plasma gas flow rate of 12 L min^{-1}.

2.2. Cell Fabrication and Charge–Discharge Testing.

We fabricated various *RE*Sb_x/Sb electrodes by a slurry coating method.[13,18,31,32] The slurry comprised of *RE*Sb_x/Sb, acetylene black (AB), carboxymethyl cellulose (CMC), and styrene–butadiene–rubber (SBR) in a weight ratio of 70:15:10:5 wt.%. We used deionized water as the dispersing agent. The prepared slurry was coated on a copper foil current collector and dried to develop the active material layer, with a mass loading and thickness of approximately 1.0 mg cm^{-2} and 8 μm, respectively.

A 2032-type coin-cell was fabricated with the slurry-coated working electrode, a K metal sheet counter electrode, and a glass fiber separator (Whatman GF/A). We utilized an ionic-liquid electrolyte composed of potassium bis(fluorosulfonyl)amide (KFSA) dissolved in *N*-methyl-*N*-propylpyrrolidinium bis(fluorosulfonyl)amide (Py13–FSA or $[C_3C_1pyrr][FSA]$). The molar ratio of KFSA to Py13–FSA was 20:80 mol%, amounting to a molar concentration of 0.9744 mol dm^{-3} (~1M) at 303 K. Detailed electrochemical and physicochemical properties of the electrolyte were previously reported.[38] The use of FSA-based electrolytes has been reported to provide remarkable superior anode properties in LIBs, NIBs, and KIBs.[29,35,39–43] Charge–discharge testing was galvanostatically performed between 0.005 and 2.000 V vs. K^+/K at 303 K with a current density of 50 or 200 mA g$(AM)^{-1}$ using an electrochemical measurement system (HJ-1001SD8, Hokuto Denko Co., Ltd.). Here, *AM* denotes the active materials including *RE*Sb_x/Sb, *RE*Sb_x, or Sb. Unless otherwise specified, the specific capacity and current density in charge-discharge curves and cycling performance were expressed as a value per *AM* weight. Cyclic voltammetry (CV)

measurement was performed between 0.005 and 2.000 V vs. K^+/K at 303 K at scan rate of 0.02 mV s^{-1} using Compactstat.h (Ivium Technologies).

2.3. Determination of Potassium Diffusion Coefficient.

The K^+ diffusion coefficient (D_{K+}) in the *RE*Sb_x was determined by a galvanostatic intermittent titration technique (GITT).[44] After the first charge-discharge cycle at a constant current density of 50 mA g(*RE*Sb_x)$^{-1}$, the GITT measurement was carried out under the following conditions; the electrode was charged at a constant current density of 25 mA g(*RE*Sb_x)$^{-1}$ for 20 min and relaxed at open circuit voltage (OCV) for 4 h.

2.4. Measurement of Reference Breaking Strength.

A reference breaking strength (C_x) of the *RE*Sb_x particles was measured by a uniaxial compression using a dynamic ultra-microhardness tester (DUH-211S, Shimadzu Co. Ltd.). Herein, the C_x is defined as the force required to the applied pressure at which a compressed *RE*Sb_x particle exhibits 10% deformation compared to its original size. The *RE*Sb_x powder was added to ethanol and dispersed by sonication. The suspension was dropped onto a glass slide and dried. The particle (diameter: d) was compressed with a plane indenter (size: 50 μm) under a test force (P) of 49 mN and a loading velocity of 2.22 mN s^{-1}. The C_x value was estimated by equation (1), where a coefficient *a* is 2.48 with the 50 μm plane indenter.

$$C_x = \frac{aP}{\pi d^2} \qquad (1)$$

3. Results and discussion

3.1. Characterization of each *RE*Sb$_x$/Sb Composite.

Figure 1a shows an XRD pattern of synthesized powder from La and Sb in a 1:1 molar ratio (blue line) and LaSb/Sb with weight ratio of 10:90 wt.% (red line). All the XRD peaks were assigned to the standard data of LaSb (ICSD No. 01-073-6810) and Sb (ICSD No. 00-005-0562) and no peaks of elemental La and Sb appeared; and thus, it is confirmed that the successful synthesis of the desired sample (LaSb/Sb composite). Figures 1b and 1c depict the SEM image and particle size distribution of LaSb/Sb powder, respectively. The LaSb/Sb composite (10/90 wt.%) was an aggregate (secondary particles) and its average particle size was 7.77 μm. Other *RE*Sb$_x$/Sb were similarly characterized (Figures S1–S4), demonstrating successful synthesis by the MA and MM treatments, with all the D_{50} values of approximately 10 μm. WD-XRF and ICP-AES analysis also demonstrated that the weight ratio of the synthesized samples closely matched the initial composition. TEM observation of LaSb/Sb composite (50/50 wt.%) revealed that the Sb and LaSb phases were homogeneously mixed at the nanosized level (Figure S5).

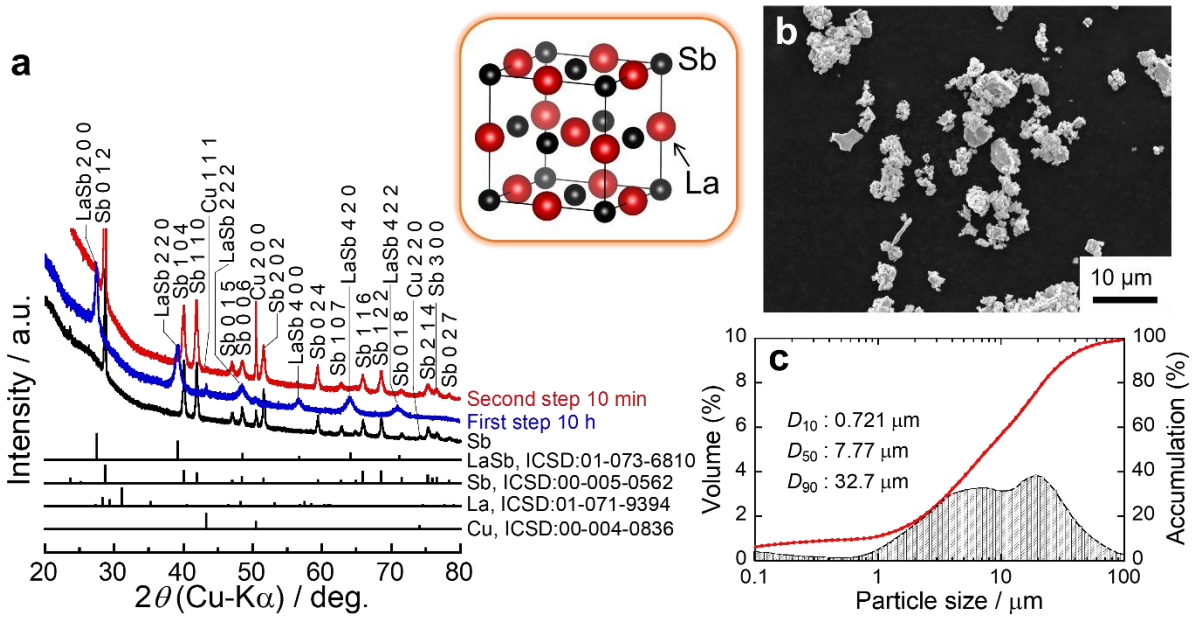

Figure 1. (a) XRD patterns of synthesized powder from La and Sb with molar ratio of 1 : 1 by MA treatment for 10 hours and from LaSb and Sb with weight ratio of 10 : 90 by MM treatment for 10 minutes. (b) SEM image and (c) particle size distribution of LaSb/Sb.

3.2. Influence of LaSb/Sb Mass Ratio on the Potassiation–Depotassiation Properties

Figure 2 shows the initial charge-discharge curve of LaSb/Sb composite electrodes with different weight ratios in 1 M KFSA/Py13-FSA at 50 mA g^{-1}. The charge (potassiation) and discharge (depotassiation) capacities increased with an increase in the amount of elemental Sb in the composite electrodes. Regardless of the weight ratio of LaSb and elemental Sb, the two potential plateaus at approximately 0.62 and 0.20 V were confirmed on the charge curves. Additionally, a potential plateau and potential shoulder appeared at around 0.61 and 1.10 V, respectively, on the discharge curve. The potential plateaus and the shoulder were confirmed on a pure Sb electrode at around above-mentioned potentials, whereas a pure LaSb electrode showed plateaus and shoulders at other potential regions. The LaSb electrode did not exhibit a distinct potential plateau but displayed potential slopes ranging from 0.49 and 0.02 V during charging and

from 0.36 and 2.00 V during discharging. Hence, it is considered that only pure Sb in the composite electrode contributes to most of the capacities.

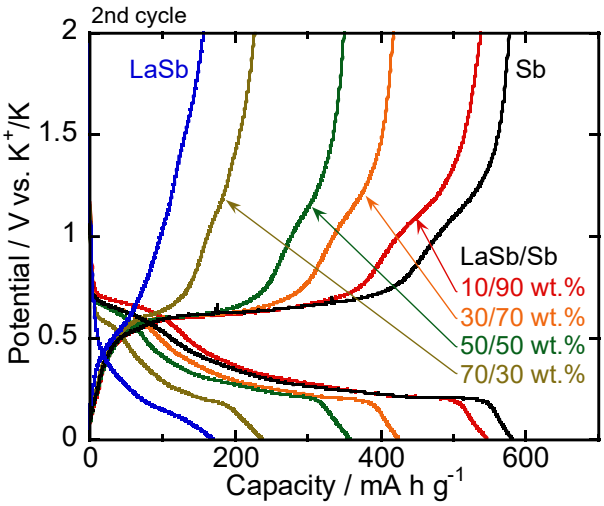

Figure 2. Charge–discharge profiles of Sb, LaSb, and LaSb/Sb electrodes of various weight ratios in 1 M KFSA/Py13-FSA at current density of 50 mA g^{-1}.

Table 1 summarized the Coulombic efficiencies (CEs) of Sb, LaSb, and LaSb/Sb composite electrodes during the initial five cycles. Comparing the CEs of the Sb and LaSb electrodes, the former exhibited higher CE over the initial five cycles. As the proportion of Sb increased, the LaSb/Sb composite electrodes with different weight ratios tended to show higher CE over the initial five cycles.

Table 1. CEs of Sb, LaSb, and LaSb/Sb electrodes (unit : %).

Cycle	Sb	LaSb	LaSb/Sb			
			10/90 wt.%	30/70 wt.%	50/50 wt.%	70/30 wt.%
1st	75.6	47.8	72.9	70.1	70.4	56.1
2nd	99.3	92.1	98.3	98.3	97.8	95.4
3rd	99.3	94.3	98.9	98.9	98.7	97.5
4th	99.1	95.3	99.1	99.3	99.1	98.4
5th	99.3	96.1	99.3	99.3	99.3	98.9

Figure 3 displays the cycling performance of LaSb/Sb composite electrodes with different weight ratios. As previously reported,[22] the pure Sb electrode had a high initial reversible capacity, whereas the reversible capacity decayed early. In contrast, we have reported that the pure LaSb electrode had only approximately a quarter of the discharge capacity of the Sb electrode but maintained its capacity stably over 400 cycles.[13] The LaSb/Sb composite electrodes suppressed the rapid capacity fading of the Sb electrode at the initial cycle regardless of the amount of LaSb added. It was demonstrated that excellent cycling stability and a high discharge capacity can be achieved even with as little as 10 wt.% of LaSb. For example, in the case of $FeSi_2$/Si composite electrodes for LIBs, $FeSi_2$ compensates for the disadvantage of Si, which has a high capacity but undergoes significant volume changes during lithiation and delithiation.[45] When the amount of $FeSi_2$ added is small, capacity decay occurs in the early stages of the cycle, similar to the pure Si electrode. However, surprisingly, the suppression of capacity decay even with as little as 10 wt.% of LaSb in this electrode system was almost identical to that confirmed at other weight ratios. Subsequent experiments used *RE*Sb_x/Sb composite electrodes with a 10/90 wt.% ratio for high-capacity applications.

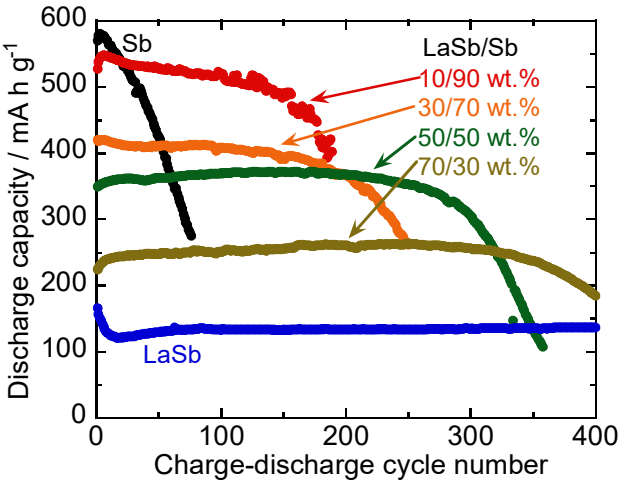

Figure 3. Cycle dependency of discharge capacities of LaSb/Sb electrodes with various weight ratios and Sb alone electrode in 1 M KFSA/Py13-FSA at a current density of 200 mA g^{-1}.

To investigate the reaction behavior of the LaSb/Sb composite electrode in detail, CV measurements of Sb, LaSb, and LaSb/Sb electrodes were performed (Figure 4). The pure Sb electrode exhibited two cathodic peaks at approximately 0.59 and 0.12 V and two anodic peaks at approximately 0.69 and 1.12 V. Each peak is attributed to the reaction shown in Figure 4a.[46,47] Additionally, each peak potential was nearly identical to the potential plateaus and shoulder of the Sb electrode shown in Figure 2. The peaks resulting from the potassiation and depotassiation of the Sb electrode appeared on the LaSb/Sb electrode. In contrast, the pure LaSb electrode showed only a cathodic peak at approximately 0.11 V, an anodic shoulder at approximately 0.38 V and three anodic peaks at approximately 0.65, 1.06, and 1.60 V. These results indicated that only Sb of the LaSb/Sb electrode alloyed and dealloyed with K, whereas the potassiation and depotassiation reactions occurred on the pure Sb and LaSb electrode. The same phenomena were confirmed on the Si-based composite electrodes for LIBs.[24,26] Due to its low formation energy,

LaSb does not undergo phase separation into La and Sb during potassiation, enabling it to reversibly store and release K^+.[13,48]

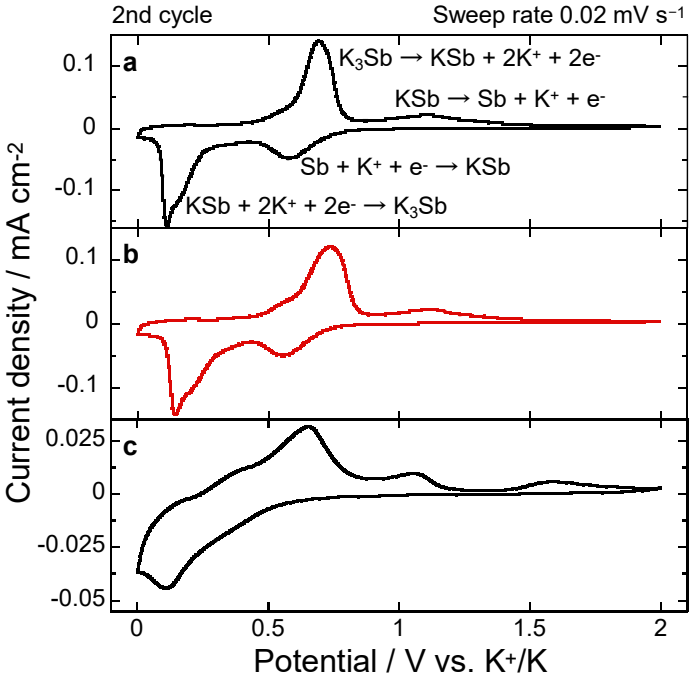

Figure 4. Cyclic voltammograms of (a) Sb, (b) LaSb/Sb (10/90 wt.%), and (c) LaSb electrodes.

3.3. Charge–Discharge Cycling Performance of Various *RE*Sb$_x$/Sb Electrodes

Figure 5 shows the charge–discharge cycle dependence of the gravimetric and volumetric discharge capacities of different *RE*Sb$_x$/Sb (10/90 wt.%) and pure Sb electrodes. The results of pure *RE*Sb$_x$ electrodes are also shown. The high density of Sb and *RE*Sb$_x$ (5.8–7.3 g cm^{-3}) resulted in a high capacity per volume. All pure *RE*Sb$_x$ electrodes exhibited long cycle stability. Among all *RE*Sb$_x$ electrodes, the CeSb and LaSb electrodes exhibited the highest and the lowest discharge capacities, respectively. The discharge capacity of the GdSb, SmSb, and YSb electrodes was comparable and the second highest. All *RE*Sb$_x$/Sb composite electrodes exhibited high initial

capacity of approximately 530 mA h g^{-1} and suppressed the rapid capacity decay of the Sb electrode at the initial cycle. In particular, the CeSb/Sb and LaSb/Sb electrodes showed superior cycle stability. It appeats that the cycling performance of *RE*Sb_x/Sb composite electrodes is not affected by the discharge capacity of pure *RE*Sb_x electrodes.

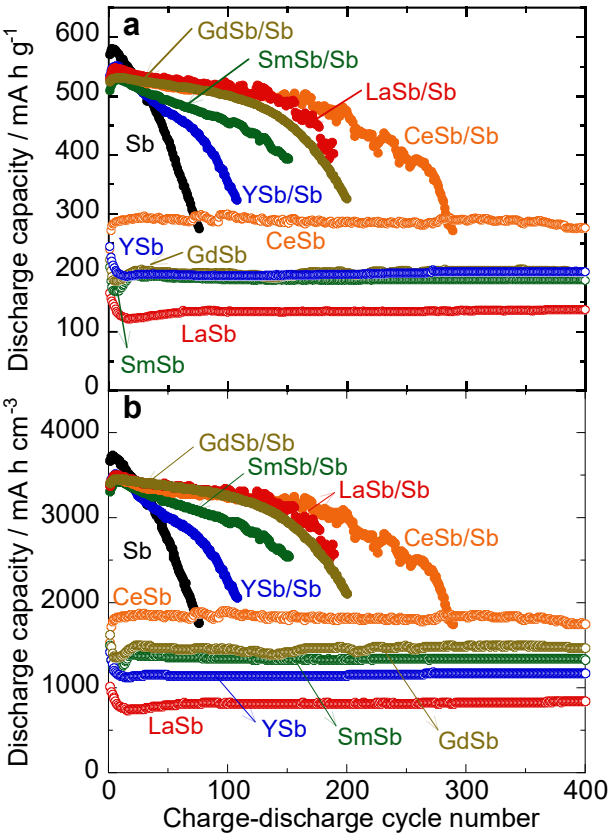

Figure 5. Cycle dependency of (a) gravimetric and (b) volumetric discharge capacities of *RE*Sb_x/Sb (10/90 wt.%) and Sb alone electrodes in 1 M KFSA/Py13-FSA at a current density of 50 mA g^{-1}.

The theoretical capacity achievement rate and the capacity retention of the *RE*Sb_x/Sb (10/90 wt.%) composite electrodes are provided in Figure S6. As mentioned above, only Sb in *RE*Sb_x/Sb (10/90 wt.%) alloyed and dealloyed with K, and hence, the theoretical capacity of the composite electrode is 594 mA h g^{-1} regardless of the *RE*Sb_x. The capacity retention also indicates

how much capacity is maintained over subsequent cycles, with the initial discharge capacity being 100%. These showed a similar trend to their cycling performances. Figure S7 also shows the capacity retention of the pure *RE*Sb_x electrodes. As can be easily seen from Figure 5, the pure *RE*Sb_x exhibited high capacity retention over 400 cycles. Figures S8 and S9 display the initial charge-discharge curve of *RE*Sb_x/Sb (10/90 wt.%) composite and pure *RE*Sb_x electrodes, respectively. For comparison, the result of the pure Sb electrode is also shown in Figure S8. Regardless of the type of *RE*Sb_x, the composite electrodes exhibited charge-discharge curves similar to those of the pure Sb electrode. Conversely, the pure *RE*Sb_x electrodes exhibited different charge-discharge behavior from that of the Sb-alone electrode. This trend was confirmed by CV measurements as shown in Figures S10-S13.

To clarify the differences in cycling performance between the different *RE*Sb_x, the cycle life tests were conducted with a charge capacity limitation of 400 mA h g^{-1} (Figure 6). To shorten the measurement time, the current density was set to 200 mA g^{-1} which is four times higher than that in the previous test. The results clearly confirmed that the cycle life depended on the *RE*Sb_x. All composite electrodes showed a longer cycle life than the pure Sb electrode. Notably, the CeSb/Sb composite electrode exhibited a cycle life more than three times longer than the pure Sb electrode. To determine the extent to which the addition of *RE*Sb_x suppresses electrode disintegration, the cause of capacity fading, SEM observations of electrode cross-sections before and after charge and discharge were performed (see the next section).

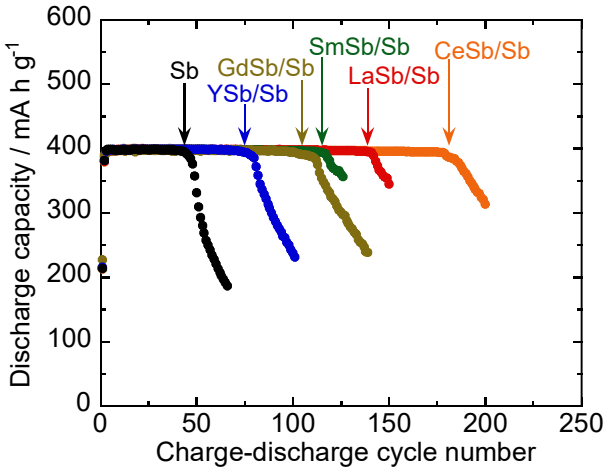

Figure 6. Cycle life of *RE*Sb$_x$/Sb (10/90 wt.%) and Sb alone electrodes in 1 M KFSA/Py13-FSA at 200 mA g^{-1} with a charge capacity limitation of 400 mA h g^{-1}.

3.4. Reaction Behaviors of *RE*Sb$_x$/Sb Electrodes

Figures 7a–7f depict the cross-sectional SEM images of the pure Sb and the *RE*Sb$_x$/Sb composite electrodes after the 50th cycle and Figure 7g shows change in the relative thickness of each electrode. Large cracks were observed at the pure Sb electrode (Figure 7a), whereas small cracks were confirmed at the composite electrodes (Figures 7b–7f) and the electrode disintegration was found to be suppressed. Figures S14–S19 display the cross-sectional SEM images of these electrodes at other cycles. It can be seen that these small cracks increased in size with an increase in the cycle number (Figures S17–S19). Additionally, the CeSb/Sb electrode with the longest cycle life continued to maintain the lowest relative thickness over all cycles. We speculated that the difference in the relative thickness was due to differences in K^+ migration ease in *RE*Sb$_x$. Thus, the D_{K+} was investigated using GITT measurements.

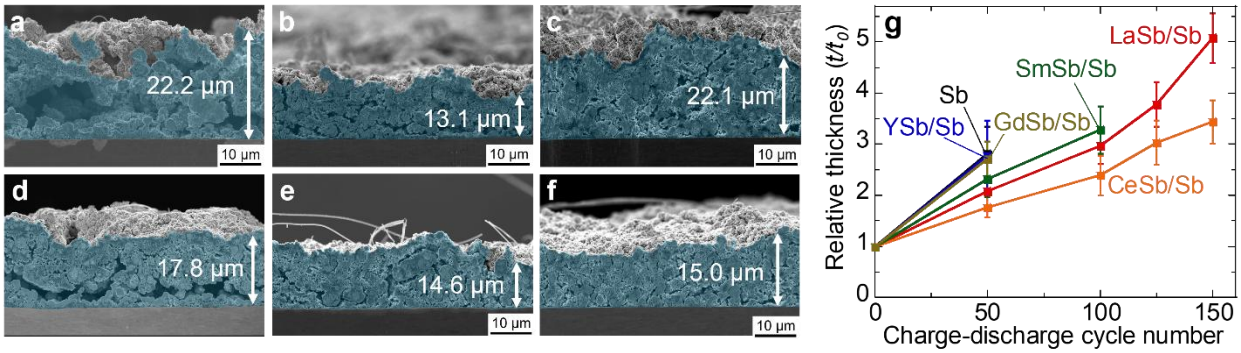

Figure 7. Cross-sectional SEM image of (a) pure Sb, (b) YSb/Sb, (c) GdSb/Sb, (d) SmSb/Sb, (e) LaSb/Sb, and (f) CeSb/Sb electrodes after 50th cycle. (g) Changes in relative thickness (t/t_0) of each electrode over the cycle. t_0 and t represent the thickness measured before and after cycling, respectively. The value of t was investigated in the depotassiation state.

Figures S20 and S21 show the relationship between the change in potential and time obtained by repeated charging and relaxation and its enlarged view of the pure Sb electrode, respectively. The D_{K+} was calculated using equation (2) and the obtained parameters of ΔE_τ and ΔE_s in Figure S21, where τ, m_B, V_m, M_B, and S means the charging time, the mass of active material, molar volume, formula weight of active material, and the area of the active material layer, respectively.

$$D_{K^+} = \frac{4}{\pi\tau}\left(\frac{m_B V_m}{M_B S}\right)^2 \left(\frac{\Delta E_S}{\Delta E_\tau}\right)^2 \qquad (2)$$

Figure 8a shows the relationship between potential and D_{K+}, whereas Figure 8b provides the correlation between the lattice parameter and the average D_{K+} at the potassiation potential of each $RESb_x$ electrode. The crystal system of all $RESb_x$ is cubic, whereas that of elemental Sb is trigonal. Table S1 summarizes the lattice parameter and potassiation potential of $RESb_x$. The D_{K+} of $RESb_x$ increased with an increase in lattice parameter. It is considered that the reason for lower D_{K+} of

pure Sb is due to a difference in the crystal structure and/or a smaller lattice constant. LaSb and CeSb particularly possess high D_{K+}, and the composite electrodes with these *RE*Sb$_x$ exhibited a superior cycle life. *RE*Sb$_x$ with high D_{K+} can function as an excellent K^+ conduction path. Thus, the disintegration of the *RE*Sb$_x$/Sb composite electrode would be suppressed by uniform K^+ storage and release throughout the electrode layer.

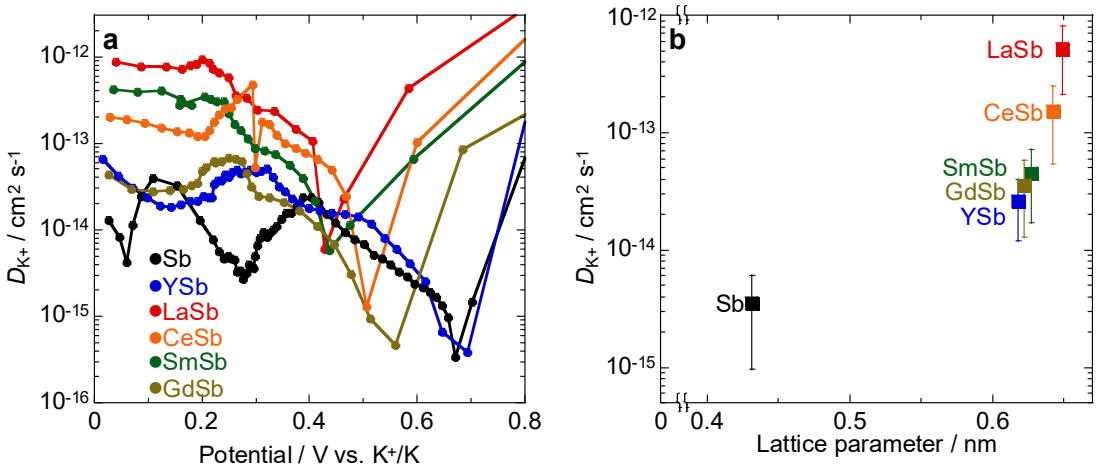

Figure 8. Relationship between (a) D_{K+} and potential and (b) D_{K+} and lattice parameter.

CeSb exhibited the longest cycle life, whereas LaSb demonstrated the highest K^+. We considered the possibility that other parameters may contribute to cycle stability and focused on the mechanical properties of the *RE*Sb$_x$, particularly the reference breaking strength, C_x. The strength is the ability to resist deformation or breakage when external forces are applied. Figure 9 shows the compressive deformation–indentation force curve and the C_x obtained for *RE*Sb$_x$ and Sb powders. Sb with the highest C_x is difficult to deform, meaning it is hard. In contrast, the *RE*Sb$_x$ with a low C_x are easily deformed, indicating that they are soft. Consequently, the CeSb was found to be the softest. It is presumed that the presence of CeSb between the hard Sb phases suppressed the pulverization of Sb and stabilized the electrode structure. Although the CeSb has slightly lower

D_{K+} than LaSb, its mechanical properties are excellent. Thus, the CeSb/Sb composite electrode is believed to exhibit excellent cycle life.

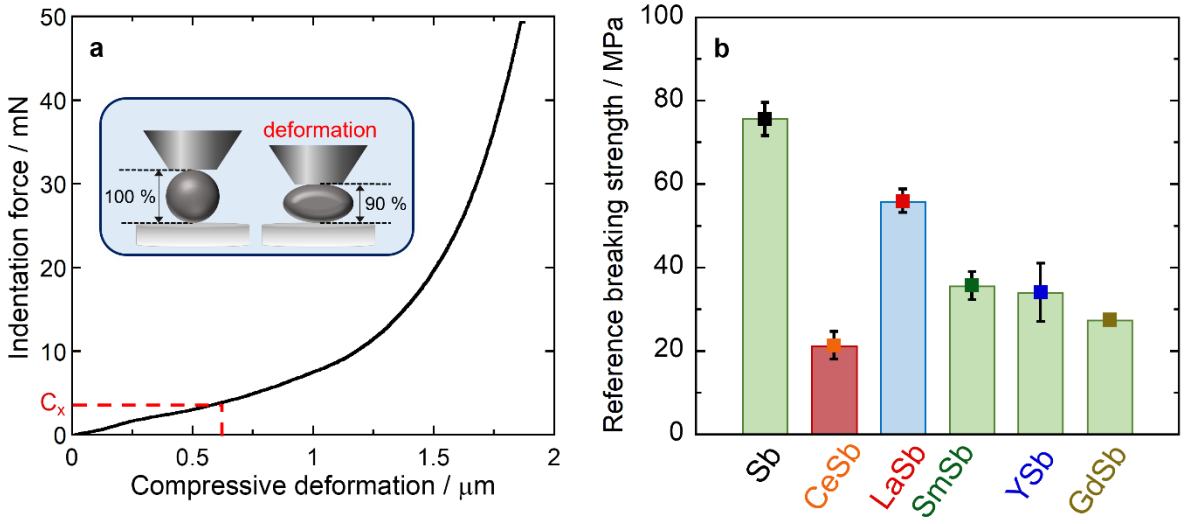

Figure 9. (a) Compressive deformation–indentation force curve and (b) reference breaking strength of *RE*Sb$_x$ and Sb powders. The inset in part (a) shows the schematic diagram of the experiment.

4. Conclusions

We investigated the electrochemical potassiation and depotassiation properties of various *RE*Sb$_x$/Sb composite electrodes in an ionic liquid electrolyte. Based on charge–discharge curves and cyclic voltammograms, only pure Sb in the composite electrode would contribute to most of the capacities. Due to the significant volumetric changes in most metal/alloy electrodes during charging and discharging, adding 10 wt.% of a substance to compensate for this drawback had little impact on the electrochemical performance. However, surprisingly, the suppression of capacity decay at 90 wt.% Sb in this electrode system was nearly identical to that at other weight ratios. The CeSb/Sb and LaSb/Sb electrodes exhibited the longest cycle life among various

*RE*Sb$_x$/Sb electrodes. The cross-sectional SEM revealed that an increase in the relative thickness of both electrodes was suppressed during charge–discharge cycling. Additionally, small cracks were observed at the *RE*Sb$_x$/Sb electrodes and large cracks were seen at the pure Sb electrode. The pure LaSb and CeSb particularly possess high D_{K+} due to their large lattice parameter. Composite electrodes with these antimonides exhibited a superior cycle life. These antimonides can function as excellent K^+ conduction paths; therefore, the disintegration of the composite electrodes was suppressed by uniform K^+ storage and release throughout the electrode layer. The CeSb/Sb electrode exhibited the longest cycle life, but the LaSb had the highest K^+. The reference breaking strength of CeSb was lower than that of LaSb, indicating that CeSb is soft and easily deformed. The presence of CeSb between the hard Sb phases stabilized the electrode structure and suppressed the pulverization of the Sb. Therefore, the CeSb/Sb composite electrode exhibited the longest cycle life.

ASSOCIATED CONTENT

Supporting Information.

XRD patterns, crystal structures, SEM images, particle size distribution, TEM image, theoretical capacity achievement rates, capacity retentions, charge–discharge curves, cyclic voltammograms, cross-sectional SEM images, GITT curves, and lattice parameters are available free of charge via the Internet at http://pubs.acs.org.

AUTHOR INFORMATION

Corresponding Authors

*Yasuhiro Domi and Hiroki Sakaguchi

E-mail: domi@tottori-u.ac.jp and sakaguch@tottori-u.ac.jp

Notes

The authors have declared no competing financial interests to report.

ACKNOWLEDGMENT

This work was partially supported by the Joint Usage/Research Program on Zero-Emission Energy Research, Institute of Advanced Energy, Kyoto University (ZE2021A-28, ZE2022A-07, and ZE2023A-21) and the NIMS Joint Research Hub Program. We thank Mr. R. Matsui of the Technical Department, Tottori University for his technical support.

Author Contributions

The manuscript was written with contributions from all authors.

REFERENCES

(1) Armand, M.; Tarascon, J.M. Building Better Batteries. *Nature* **2008,** *451* (7179), 652–657. DOI: 10.1038/451652a

(2) Whittingham, M.S. Lithium Batteries and Cathode Materials. *Chem. Rev.* **2004,** *104* (10), 4271–4301. DOI: 10.1021/cr020731c

(3) Goodenough, J.B.; Kim, Y. Challenges for Rechargeable Li Batteries. *Chem. Mater.* **2010,** *22* (3), 587–603. DOI: 10.1021/cm901452z

(4) Yabuuchi, N.; Kubota, K.; Dahbi, M.; Komaba, S. Research Development on Sodium–Ion Batteries. *Chem. Rev.* **2014,** *114* (23), 11636–11682. DOI: 10.1021/cr500192f

(5) Hwang, J.-Y.; Myung, S.-T.; Sun, Y.-K. Sodium-Ion Batteries: Present and Future. *Chem. Soc. Rev*. **2017**, *46* (12), 3529–3614. DOI: 10.1039/c6cs00776g

(6) Komaba, S. Sodium-Driven Rechargeable Batteries: An Effort Towards Future Energy Storage. *Chem. Lett.* **2020,** *49* (12), 1507–1516. DOI: 10.1246/cl.200568

(7) Tian, Y.; Zeng, G.; Rutt, A.; Shi, T.; Kim, H.; Wang, J.; Koettgen, J. Sun, Y.; Ouyang, B.; Chen, T.; Lun, Z.; Rong, Z.; Persson, K.; Ceder, G. Promises and Challenges of Next-Generation "Beyond Li-ion" Batteries for Electric Vehicles and Grid Decarbonization. *Chem. Rev*. **2021**, *121* (3), 1623–1669. DOI: 10.1021/acs.chemrev.0c00767

(8) Eftekhari, A.; Jian, Z, Ji, X. Potassium Secondary Batteries. *ACS Appl. Mater. Interfaces* **2017**, *9* (5), 4404–4419. DOI: 10.1021/acsami.6b07989

(9) Wu, X.; Leonard, D. P.; Ji, X. Emerging Non-Aqueous Potassium-Ion Batteries: Challenges and Opportunities. *Chem. Mater.* **2017,** *29* (12), 5031–5042. DOI: 10.1021/acs.chemmater.7b01764

(10) Hosaka, T.; Kubota, K.; Hameed, A. S.; Komaba, S. Research Development on K-Ion Batteries. *Chem. Rev.* **2020,** *120* (14), 6358–6466. DOI: 10.1021/acs.chemrev.9b00463

(11) Luo, W.; Shen, F.; Bommier, C.; Zhu, H.; Ji, X.; Hu, L. Na-Ion Battery Anodes: Materials and Electrochemistry. *Acc. Chem. Res*. **2016**, *49* (2), 231–240. DOI: 10.1021/acs.accounts.5b00482

(12) Li, Y.; Lu, Y.; Adelhelm, P.; Titirici, M.-M., Hu, Y.-S. Intercalation Chemistry of Graphite: Alkali Metal Ions and Beyond. *Chem. Soc. Rev*. **2019**, *48* (17), 4655–4687. DOI: 10.1039/C9CS00162J

(13) Domi, Y.; Usui, H.; Kuritani, K.; Wada, N.; Nishikawa, K.; Yamamoto, T.; Nohira, T.; Sakaguchi, H. Anode Properties of Sb-Based Alloy Electrodes for K‑Ion Batteries in an Ionic-Liquid Electrolyte. *ACS Appl. Energy Mater.* **2023**, *6* (22), 11583–11591. DOI: 10.1021/acsaem.3c02002

(14) Jian, Z.; Luo, W.; Ji, X. Carbon Electrodes for K-Ion Batteries. *J. Am. Chem. Soc.* **2015,** *137* (36), 11566–11569. DOI: 10.1021/jacs.5b06809

(15) Igarashi, D.; Kubota, K.; Hosaka, T.; Tatara, R.; Inose, T.; Ito, Y.; Inoue, H.; Takeuchi, M.; Komaba, S. Effect of Crystallinity of Synthetic Graphite on Electrochemical Potassium Intercalation into Graphite. *Electrochemistry* **2021**, *89* (5), 433–438. DOI: 10.5796/electrochemistry.21-00062

(16) Onuma, H.; Kubota, K.; Muratsubaki, S.; Ota, W.; Shishkin, M.; Sato, H.; Yamashita, K.; Yasuno, S.; Komaba, S. Phase Evolution of Electrochemically Potassium Intercalated Graphite. *J. Mater. Chem. A* **2021,** *9* (18), 11187–11200. DOI: 10.1039/d0ta12607a

(17) Zhang, W.; Mao, J.; Li, S.; Chen, Z.; Guo, Z. Phosphorus-Based Alloy Materials for Advanced Potassium-Ion Battery Anode. *J. Am. Chem. Soc.* **2017**, 139 (9), 3316–3319. DOI: 10.1021/jacs.6b12185

(18) Domi, Y.; Usui, H.; Nakabayashi, E.; Yamamoto, T.; Nohira T.; Sakaguchi, H. Potassiation and Depotassiation Properties of Sn_4P_3 Electrode in an Ionic-Liquid Electrolyte. *Electrochemistry* **2019,** *87* (6), 333–335. DOI: 10.5796/electrochemistry.19-00052

(19) Xiong, P.; Wu, J.; Zhou, M.; Xu, Y. Bismuth-Antimony Alloy Nanoparticle@Porous Carbon Nanosheet Composite Anode for High-Performance Potassium-Ion Batteries. *ACS Nano* **2020,** *14* (1), 1018–1026. DOI: 10.1021/acsnano.9b08526

(20) Hsieh, Y.-Y.; Chen, K.-T.; Tuan, H.-Y. A Synergetic SnSb-Amorphous Carbon Composites Prepared from Polyesterification Process as an Ultrastable Potassium-Ion Battery Anode. *Chem. Eng. J.* **2021,** *420* (3), 130451. DOI: 10.1016/j.cej.2021.130451

(21) Gao, H.; Wang, Y.; Guo, Z.; Yu, B.; Cheng G.; Yang, W.; Zhang, Z. Dealloying-Induced Dual-Scale Nanoporous Indium-Antimony Anode for Sodium/Potassium Ion Batteries. *J. Energy Chem.* **2022,** *75*, 154–163. DOI: 10.1016/j.jechem.2022.08.016

(22) Wu, Y.; Sun, Y.; Tong, Y.; Li, H. $FeSb_2$ Nanoparticles Embedded in 3D Porous Carbon Framework: An Robust Anode Material for Potassium Storage with Long Activation Process. *Small* **2022,** *18* (24), 2201934. DOI: 10.1002/smll.202201934

(23) Wang, Z.; Qiao, S.; Ma, M.; Li, T.; Liu, J. K.; Dou, S. X.; Chong, S. High-Entropy Conversion-Alloying Anode Material for Advanced Potassium-Ion Batteries. *ACS Nano* **2025**, *19* (15), 15148–15160. DOI: 10.1021/acsnano.5c03792

(24) Domi, Y.; Usui, H.; Shindo, Y.; Yodoya, S.; Sato, H.; Nishikawa, K.; Sakaguchi, H. Electrochemical Lithiation and Delithiation Properties of $FeSi_2$/Si Composite Electrodes in Ionic-Liquid Electrolytes. *Electrochemistry* **2020**, *88* (6), 548–554. DOI: 10.5796/electrochemistry.20-00091

(25) Usui, H.; Domi, Y.; Uehara, I.; Itoda, Y.; Iwama, E.; Oishi, N.; Nitta, N.; Sakaguchi, H. Cyclability Enhancement of CeO_2/Sb_2O_3 Composite Electrode via Ternary Na-Storage Reactions. Ceram. Int. 2022, 48 (23), 35593–35598. DOI: 10.1016/j.ceramint.2022.08.268

(26) Domi, Y.; Usui, Okasaka, T.; Nishikawa, K.; Sakaguchi, H. Silicon-Based Nanocomposite Anodes with Excellent Cycle Life for Lithium-Ion Batteries Achieved by the Synergistic Effect of Two Silicides. *J. Electrochem. Soc.* **2024**, *171* (8), 080506. DOI: 10.1149/1945-7111/ad69c6

(27) Domi, Y.; Usui, Sakaguchi, H. Analysis of the Interfacial Reaction between Si-Based Anodes and Electrolytes in Li-Ion Batteries. *Chem. Commun.* **2024**, *60* (89), 12986–12999. DOI: 10.1039/d4cc04134h

(28) Watanabe, H.; Usui, H.; Domi, Y.; Iwama, E.; Kurokawa, H.; Sakaguchi, H. Effect of Composite Formation with Various Metals on Improving the Anode Performance of Hematite for Na-Ion Batteries. *ACS Appl. Energy Mater*. **2024**, *7* (7), 2973–2979. DOI: 10.1021/acsaem.4c00358

(29) Usui, H.; Domi, Y.; Fujiwara, K.; Shimizu, M.; Yamamoto, T.; Nohira, T.; Hagiwara, R.; Sakaguchi, H. Charge–Discharge Properties of Sn_4P_3 Negative Electrode in Ionic Liquid Electrolyte for Na-Ion Batteries. *ACS Energy Lett*. **2017**, *2* (5), 1139–1143. DOI: 10.1021/acsenergylett.7b00252

(30) Usui, H.; Domi, Y.; Yamagami, R.; Fujiwara, K.; Nishida, H.; Sakaguchi, H. Sodiation–Desodiation Reactions of Various Binary Phosphides as Novel Anode Materials of Na-Ion Battery. *ACS Appl. Energy Mater*. **2018**, *1* (2), 306–311. DOI: 10.1021/acsaem.7b00241

(31) Usui, H.; Domi, Y.; Takada, N.; Sakaguchi, H. Reaction Mechanism of Indium Antimonide as a Sodium Storage Material. *Cryst. Growth Des*. **2021**, *21* (1), 218–226. DOI: 10.1021/acs.cgd.0c01045

(32) Domi, Y.; Usui, H.; Ando, T; Tanaka, R.; Gotoh, K.; Hoshi, T.; Nishikawa, K.; Sakaguchi, H. Electrochemical Lithiation Mechanism of Nickel Silicide Electrode. *Electrochemistry* **2025**, *93* (3), 037009. DOI: 10.5796/electrochemistry.25-00015

(33) Domi, Y.; Usui, H.; Shimizu, M.; Kakimoto, Y.; Sakaguchi, H. Effect of Phosphorus-Doping on Electrochemical Performance of Silicon Negative Electrodes in Lithium-Ion Batteries. *ACS Appl. Mater. Interfaces* **2016**, *8* (11), 7125–7132. DOI: 10.1021/acsami.6b00386

(34) Yodoya, S.; Domi, Y.; Usui, H.; Sakaguchi, H. Applicability of an Ionic Liquid Electrolyte to a Phosphorus-Doped Silicon Negative Electrode for Lithium-Ion Batteries. *ChemistrySelect* **2019**, *4* (4), 1375–1378. DOI: 10.1002/slct.201803282

(35) Domi, Y.; Usui, H.; Yamaguchi, K.; Yodoya, S.; Sakaguchi, H. Silicon-Based Anodes with Long Cycle Life for Lithium-Ion Batteries Achieved by Significant Suppression of Their Volume Expansion in Ionic-Liquid Electrolyte. *ACS Appl. Mater. Interfaces* **2019,** *11* (3), 2950–2960. DOI: 10.1021/acsami.8b17123

(36) Usui, H.; Domi, Y.; Nguyen, T. H.; Tanaka, Y.; Sakaguchi, H. Indium-Doped Rutile Titanium Oxide with Reduced Particle Length and Its Sodium Storage Properties. *ACS Omega* **2020**, *5* (25), 15495−15501. DOI: 10.1021/acsomega.0c01623

(37) Hirono, T.; Usui, H.; Domi, Y.; Irie, W.; Nishida, T.; Sawada, T.; Sakaguchi, H. Effect of Sn Addition on Anode Properties of SiO_x in Sodium-Ion Batteries. *Electrochemistry* **2023**, *91* (1), 017001. DOI: 10.5796/electrochemistry.22-00123

(38) Yamamoto, T.; Matsumoto, K.; Hagiwara, R.; Nohira T. Physicochemical and Electrochemical Properties of K[$N(SO_2F)_2$]-[*N*-Methyl-*N*-propylpyrrolidinium][$N(SO_2F)_2$] Ionic Liquids for Potassium-Ion Batteries. *J. Phys. Chem. C* **2017**, *121* (34), 18450–18458. DOI: 10.1021/acs.jpcc.7b06523

(39) Domi, Y.; Usui, H.; Ieuji, N.; Nishikawa, K.; Sakaguchi, H. Lithiation/Delithiation Properties of Lithium Silicide Electrodes in Ionic-Liquid Electrolytes. *ACS Appl. Mater. Interfaces* **2021**, *13* (3), 3816–3824. DOI: 10.1021/acsami.0c17552

(40) Yamamoto, T.; Yadav, A.; Nohira T. Charge–Discharge Behavior of Graphite Negative Electrodes in FSA-Based Ionic Liquid Electrolytes: Comparative Study of Li-, Na-, K-Ion Systems. *J. Electrochem. Soc.* **2022**, *169* (5), 050507. DOI: 10.1149/1945-7111/ac6a1a

(41) Jiao, K.; Yamamoto, T.; Kiuchi, H.; Zhao, H.; Nohira T. Mn-Based Transition Metal Oxide Positive Electrode for K-Ion Battery Using an FSA-Based Ionic Liquid Electrolyte. *J. Electrochem. Soc.* **2024**, *171* (10), 100510. DOI: 10.1149/1945-7111/ad803a

(42) Ishio, Y.; Yamamoto, T.; Manabe, K.; Nohira T. In-Situ Raman Spectroscopic Analysis of Factors Improving Discharge Rate Capability of Na-Ion Batteries with FSA-Based Ionic Liquids. *Electrochemistry* **2024**, *92* (4), 043017. DOI: 10.5796/electrochemistry.23-69166

(43) Jiao, K.; Yamamoto, T.; Nohira T. Comparative Study of Layered Manganese-based Oxides Doped with Iron, Titanium, and Aluminum: Positive Electrode Performance in K-Ion Battery Using an Ionic Liquid Electrolyte. *Electrochemistry* **2025**, *93* (2), 027006. DOI: 10.5796/electrochemistry.24-00102

(44) Huang, Z.; Wang, Z.; Guo, H.; Li, X. Influence of Mg^{2+} Doping on the Structure and Electrochemical Performances of Layered $LiNi_{0.6}Co_{0.2-x}Mn_{0.2}Mg_xO_2$ Cathode Materials. *J Alloys and Compd*. **2016**, *671* (25) 479–485. DOI: 10.1016/j.jallcom.2016.02.119

(45) Usui, H.; Nouno, K.; Takemoto, Y.; Nakada, K.; Ishii, A.; Sakaguchi, H. Influence of Mechanical Grinding on Lithium Insertion and Extraction Properties of Iron Silicide/Silicon Composites. *J. Power Sources* **2014**, *268* (5), 848–852. DOI: 10.1016/j.jpowsour.2014.06.105

(46) McCulloch, W. D.; Ren, X.; Yu, M.; Huang, Z.; Wu, Y. Potassium-Ion Oxygen Battery Based on a High Capacity Antimony Anode. *ACS Appl. Mater. Interfaces* **2015**, *7* (47), 26158–26166. DOI: 10.1021/acsami.5b08037

(47) Nazir, A.; Le, H. T. T.; Nguyen, A.-G.; Kim, J.; Park, C.-J. Conductive Metal Organic Framework Mediated Sb Nanoparticles as High-Capacity Anodes for Rechargeable Potassium-Ion Batteries. *Che. Eng. J.* **2022**, *450* (4), 138408. DOI: 10.1016/j.cej.2022.138408

(48) Schlesinger, M. E.; Thermodynamic Properties of Solid Binary Antimonides. *Chem. Rev*. **2013**, *113* (10), 8066–8092. DOI: 10.1021/cr400050e

BRIEFS (Word Style “BH_Briefs”).